

# PROFILES OF WIND DIRECTION AND SPEED IN TURBULENT EKMAN FLOW

CEDRICK ANSORGE, HAUKE WURPS

**ABSTRACT.** The profiles of wind speed and direction in turbulent Ekman flow are formulated based on asymptotic theory and data from direct numerical simulation. The profile of the streamwise component follows the classical viscous, logarithmic and wake scaling. In the outer layer, the velocity component profiles can be described by an Ekman-spiral with adapted boundary conditions that result in a reduction of the spiral-like rotation. The span-wise component poses a conceptual challenge to the channel-flow analogy in the context of asymptotic matching; it exhibits a mixed scaling in the surface layer, but follows outer scaling for most of the outer layer. Viscous stress scales universally across the boundary layer in inner units while the total stress becomes universal as a function of outer height. This implies a mixed scaling for the turbulent stress and eddy viscosity across the inner layer and convergence to a universal scaling as function of the outer height across the outer layer for increasing scale separation *vide* Reynolds numbers.

## 1. INTRODUCTION

Wind veer away from its geostrophic direction is (i) due to direct frictional effects in the very vicinity of the surface and (ii) due to turbulence which exerts indirect frictional effects; these effects cause a slow-down of the mean wind reducing the Coriolis force thus turning the wind in favor of the pressure gradient force. Not only does the veering set the frame of reference for surface layer theory, it also has effects at small and large scales. From a large-scale perspective, the veering of wind across the planetary boundary layer determines the amount of cross-isobaric mass-flux, commonly referred to as 'Ekman pumping' (Ekman, 1905), and it is thus a key factor in the life-cycle of large-scale synoptic systems. At the small-scale end, the directional shear of the wind in the upper part of the surface layer may cause a systematic yaw for tall wind power generation devices where blades reach into the Ekman layer, i.e. that part of the boundary layer where the wind starts to turn.

In the planetary boundary layer, wind veer is characterized by the surface veering angle  $\alpha$  defined as the angle between the negative surface shear stress  $\tau_{\text{sfc}}$  and the geostrophic wind. Surface veering  $\alpha$  and geostrophic drag  $Z \equiv u_*/G$ , where  $u_* \equiv \sqrt{\nu|\tau_{\text{sfc}}|}$ , uniquely determine the surface drag  $\tau_{\text{sfc}}$  in a turbulent Ekman flow. In any quantitative description of the surface layer, the friction velocity  $u_*$  is the dynamic scale and  $\alpha$  defines the alignment of the frame of reference. Knowledge about  $u_*$  and  $\alpha$  is thus a pre-requisite for any quantitative theory of the surface layer and a first attempt in theoretical quantification was undertaken by Rossby and Montgomery (1935) using integral relations in the boundary layer. Asymptotic similarity theory was later used by Tennekes (1973) and Blackadar and Tennekes (1968), and—based on his seminal direct numerical simulations (DNS) of Ekman

flow-, Spalart, 1989 suggested a modification to take into account effects of low to intermediate Reynolds numbers. Later on, constants were re-evaluated with a focus on the atmospheric boundary layer based on observations (Högström, 1988; Högström, 1996) and numerical modelling (Spalart et al., 2008; Spalart et al., 2009; Ansorge and Mellado, 2014; Ansorge, 2019).

Attempts were also undertaken to obtain profiles of the wind speed: One approach is to match the inner and outer layer at a reference height; Etling (2002) and Emeis (2018) (Sec. 21.10; Eq. 21.48) choose the Prandtl-layer height to match the wind speed profiles, which, however, requires to externally prescribe the veering  $\alpha$  at that height. A one-dimensional profile with constant veering is given by Emeis et al. (2007, Sec. 3, Eq. 3.1-3.19).

Gryning et al. (2007) present an extension of the wind-speed profile beyond the surface layer using a neutral reference profile and a stability correction; Kelly and Gryning, 2010, based on a probabilistic representation of stratification, develop a model for the long-term mean windspeed in the atmospheric boundary layer and compare this with observation at different sites; Kelly and Troen, 2016 demonstrate the effect of such improved model for wind-energy applications. In consideration of the large scale separation in geophysical flow, the rotation of the wind in the surface layer is often assumed negligible, and above investigations merely focus on the wind speed; that means, the veering of the wind with height is not described and there is little knowledge on the profile of the span-wise velocity component and the precise shape of the hodograph in the limit of a truly neutral Ekman boundary layer.

Ekman-layer models and two-layer models of the ABL take into account rotational effects at higher altitudes, for instance when the wind speed needs to be evaluated at heights on the order of 100-200 m, a particular concern when it comes to wind-power forecasting (Optis et al., 2014). Despite rotational effects being considered, the formulation of these models for the outer layer and analysis of their performance primarily focuses on wind speed. Still, in 2018, Jiang et al. recognized that the outer part of the Ekman boundary layer receives less attention in comparison with the surface layer and commence in studying the neutral problem by Large-Eddy simulation (LES). They focus on the wind speed and find an extended logarithmic layer when considering the wind speed instead of the shear-aligned component, and they eventually demonstrate by means of an analytical model that this vertical extension of the logarithmic layer may be explained by a transfer of stress to the spanwise velocity component where it is assumed that the shear vector  $\tau(z)$  and stress vectors  $(\partial_z U, \partial_z V)$  are aligned.

Turbulent Ekman flow is considered here as a conceptual model of the homogeneous, stationary atmospheric boundary layer over a flat surface under neutral stratification. Universal profiles of the wind vector for turbulent Ekman flow not only are a well-described limit for theoretical exploration or higher-order approaches taking into account possible effects of stratification, roughness or other physical complications encountered in the realgeophysical system. While, on first sight, the study of such a strongly idealized case appears as an academic problem, it contains the essence of surface similarity as it is used in most atmospheric models, be it conceptual or numeric ones. For instance, effects of roughness are commonly incorporated by a linear transformation of vertical scale involving the roughness parameter  $z_0$  and for larger roughness also a displacement height (Monin and Yaglom, 1975; Jacobs and Van Boxel, 1988; Högström, 1988); effects of stability are commonly accounted for by

a linearization around the neutrally stratified profile (Monin, 1970; Monin and Yaglom, 1975; Högström, 1988; Högström, 1996; Sakagami et al., 2020). Furthermore, profiles can serve as better initial condition for numerical simulation of the flow, to minimize the length of initial transient periods, or as benchmark for turbulence closures that can be tuned to reproduce the neutral limit case.

Despite the strong simplifications implied by our choice of set-up, there is no straightforward approach to solving this conceptually well-defined problem. Large-Eddy simulation not only needs to be tuned for the surface shear stress and veering angle, but it also relies on sub-grid closures that often assume alignment of the stress with gradients – a questionable pre-requisite when the wind rotates with height. Esau (2004) investigated the representation of the Ekman boundary layer by dynamical subgrid closures and Zikanov et al., 2003 proposed a closure for the wind profile using a linearized representation of the eddy viscosity. Despite advances in analysis of this simplified set-up (Jiang et al., 2018), there is yet insufficient understanding for a quantitative generalization of the results to arbitrary external forcing (manifest in variation of the Reynolds number) – and indeed the fundamental questions pertaining to such relatively simple dynamics of turbulence are not reflected in the research foci of LES for the ABL over the past 50 years (Stoll et al., 2020).

At the same time, an increasing amount of high-quality and high-resolution data from turbulence-resolving approaches is emerging due to recent advances in high-performance computing and its application to geophysical problem sets; the geophysical range of scale separation, however, is—and it will remain so for the foreseeable future—out of reach for such simulation (Dimotakis, 2005). Here, the routinely employed concept of Reynolds-number similarity can help. It postulates the existence of “*fully developed turbulence*” believed to occur for a sufficiently large but finite Reynolds number” (Barenblatt and Goldenfeld, 1995). (Already in 1998, this in fact lead Moin and Mahesh to the question *how high a Re is high enough?*) In fully developed turbulence certain statistics such as dissipation (Dimotakis, 2005) or profiles of mean velocity (Barenblatt, 1993) become independent of the Reynolds number when scaled appropriately while other statistics, such as the near-wall maximum in velocity fluctuation depend on Re (Baars and Marusic, 2020) and external interfaces may exert an impact on near-wall scaling (Silva et al., 2014). It appears that for certain statistics in Ekman flow, fully-developed turbulence is reached with the Reynolds numbers that became possible with the increasing capabilities of supercomputing over the past decades.

This paper exploits the robust features of mean velocity profiles from direct numerical simulation across a range of Reynolds numbers to formulate both the streamwise and span-wise components of the mean velocity vector as a function of the Reynolds number.

## 2. PROBLEM FORMULATION AND NUMERICAL APPROACH

We consider here incompressible, turbulent Ekman flow, that is, the turbulent flow over a flat rotating plate, as a physical model for the truly neutral atmospheric boundary layer (ABL). The f-plane approximation is applied such that rotation only acts on horizontal velocity components; we thus neglect rotational effects on the horizontal components of velocity and dynamical effects due to latitudinal variation of the rate of rotation.

**2.1. Notation and Governing Equations.** The dimensional velocity vector of the numerical simulations is  $\underline{U} = (U_1, U_2, U_3) = (U, V, W)$  over the coordinate system  $Oxyz$ , where an approximate alignment (plus/ minus few degrees) of the direction  $Ox$  with the surface shear stress is achieved. The coordinate  $Oz$  points away from the wall, and  $Oy$  points in the span-wise direction normal to  $Oxz$ . For analysis of the results, we use two coordinate systems that are (i) exactly aligned with the surface shear stress

$$(1a) \quad \underline{\tau}_{\text{sfc}} = \begin{pmatrix} \tau_x \\ \tau_y \\ \tau_z \end{pmatrix} = -\nu \left( \frac{\partial U}{\partial z} \hat{e}_x + \frac{\partial V}{\partial z} \hat{e}_y \right)$$

and labelled by an upper index  $\alpha$  as in  $\underline{U}^\alpha$  for the velocity vector, and (ii) the coordinate system aligned with the free-atmosphere geostrophic wind labelled by an upper index  $G$  as in  $\underline{U}^G$ . We denote the modulus of the surface shear, the surface friction, by

$$(1b) \quad u_* = \sqrt{\|\underline{\tau}_{\text{sfc}}\|}$$

and let  $Z_* = G/u_*$ ; the surface veering angle  $\alpha_*$  is the angle between  $\underline{\tau}$  and the geostrophic wind

$$(1c) \quad \alpha_* = \sphericalangle(\underline{G}, \underline{\tau}_{\text{sfc}}).$$

Analogously, we denote the height-local veering of the wind  $\alpha(z) = \sphericalangle(\underline{G}, \underline{U}(z))$ .

We consider the incompressible Navier–Stokes equations for the three velocity components on the f-plane in a framework that is governed by the physical parameters (i) geostrophic wind magnitude  $G = \sqrt{G_1^2 + G_2^2}$  (where  $\mathbf{G} = (G_1, G_2, 0)$  is the geostrophic wind vector), (ii) Coriolis parameter  $f$  (representing the angular rotation), and (iii) kinematic viscosity  $\nu$ . In absence of external variability, this system converges to a statistically steady state in the sense that flow statistics do not depend on time; and this state is defined by a Reynolds number, the only non-dimensional parameter that governs the system. We use the geostrophic wind as velocity and the Coriolis parameter  $f$  as time scale for the non-dimensional framework. This implies the Rossby radius  $\Lambda_{\text{Ro}} = G/f$  as length scale, such that one Reynolds number governing the problem reads as

$$(2) \quad \text{Re}_\Lambda = \frac{G\Lambda_{\text{Ro}}}{\nu}.$$

The scales used in defining  $\text{Re}_\Lambda$  loose their relevance in describing the turbulent state of the flow. The friction Reynolds number

$$(3) \quad \text{Re}_\tau = \frac{u_* \delta}{\nu} = \delta^+ = \frac{\text{Re}_\Lambda}{Z_*^2},$$

where  $\delta = u_*/f$  and we use a superscript '+' to denote normalization by inner turbulence scales  $(u_*, \nu)$ .  $\text{Re}_\tau$  is suitable to compare the turbulence scale separation also to other wall-bounded flow geometries such as rotating or non-rotating channel, pipe, or Couette flow.

The governing equations non-dimensionalized by  $G$ ,  $f$ , and  $\Lambda_{\text{Ro}}$  read as

$$(4a) \quad \frac{\partial u_i}{\partial t} = \frac{\partial \pi}{\partial x_i} - u_j \frac{\partial u_i}{\partial x_j} + \epsilon_{ij} (u_j - G_j) + \frac{1}{\text{Re}} \frac{\partial^2 u_i}{\partial x_j^2}$$

$$(4b) \quad \frac{\partial u_j}{\partial x_j} = 0,$$

TABLE 1. Direct numerical simulation datasets used in this work

$\text{Re}_\Lambda$	$\text{Re}_D$	$L_{xy}/\Lambda$	$N_x \times N_y \times N_z$	$\Delta x^+$	$\Delta y^+$	$\Delta z^+ _{z=0}$
125 000	500	1.08	$2048 \times 2048 \times 192$	4.1	4.1	1.05
281 250	750	1.08	$3072 \times 3072 \times 384$	5.6	11.2	1.60
500 000	1 000	1.08	$3072 \times 6144 \times 512$	9.3	4.7	1.14
845 000	1 300	0.54	$2560 \times 5120 \times 640$	8.9	4.5	0.99
1 280 000	1 600	0.54	$3860 \times 7680 \times 960$	8.6	4.3	1.00

where  $u_i = U_i/G$  are the non-dimensional components velocity,  $\pi$  is non-dimensional pressure, and  $g_j = G_j/G$  are non-dimensionalized components geostrophic wind (with  $g_1^2 + g_2^2 = 1$  by construction). These equations are solved inside a bounded cube of size  $L_x \times L_y \times L_z$  with periodic boundary conditions in the lateral directions  $Oxy$ , a no-slip–no-penetration boundary at  $z = 0$ , and a no-penetration, free-slip boundary at  $z = L_z$ .

**2.2. Numerical Simulations.** The problem is solved numerically by tLab<sup>1</sup>, an open-source tool-suite to simulate and analyze turbulent flows. We use here a fourth-order–five-step Runge–Kutta integration and sixth-order compact schemes for spatial derivatives in all directions. The incompressibility constraint is enforced by a fractional step approach where the Poisson equation for the pressure field is solved to machine accuracy using a combined spectral/compact approach as described in Mellado and Ansorge (2012).

Simulations used here are shown in Tab. 1. We extend an existing set of simulations for  $\text{Re}_\Lambda \in \{125\,000; 281\,250; 500\,000\}$  (gray shading; cf. Ansorge and Mellado, 2014; Ansorge and Mellado, 2016) by new simulations at higher Reynolds numbers up to  $\text{Re}_\Lambda = 1.28 \times 10^6$  with a horizontal domain extent up to  $3.3 \times 10^4$  viscous units. In total, this yields one order of magnitude variation in terms of the scale separation in the boundary layer.

### 3. SCALING BEHAVIOR OF THE FLOW FOR $\text{Re}_\tau$ UP TO 3000

The generalization of profiles to arbitrary Reynolds numbers requires sufficient scale separation in the simulations, not only to quantify the effect of the Reynolds number on low-order flow statistics, but also to assess the corresponding rate-of-change to eventually allow for an extrapolation of the findings. While the simulations previously available (gray shading in Tab. 1) give confidence in a first-order representation of the turbulent problem, the estimation of higher-order effects such as the dependency of the Reynolds number requires a broader scale separation that is made available by the two new simulations for (cf. Tab. 1). Data at such scale separation has been obtained previously (cf. Spalart et al., 2008; Spalart et al., 2009), but we also need high confidence with respect to the convergence of simulation data for slow oscillations and with respect to sampling convergence, which translates to two further requirements on the data: First, data should be free of artifacts from long-term oscillations across the vertical extent of the domain—primarily, simulations should be free of effects originating from the inertial oscillation; this is achieved here

<sup>1</sup><https://github.com/turbulencia/tlab>

TABLE 2. Bulk characterization of the simulations for different Reynolds numbers  
 Viscous Reynolds number  $Re$ , friction Reynolds number  $Re_\tau$ , friction velocity  $u_*$ ,  
 surface veering angle  $\alpha_*$ , normalized boundary layer depth  $\delta_{95}/\delta$  inner normalization  
 of vertically integrated TKE, outer normalization of vertically integrated dissipation.

$Re$	$\delta^+ = Re_\tau$	$u_*$	$\alpha_*$	$\delta_{95}/\delta$	$f u_*^{-3} \int_0^\delta \epsilon dz$	$G^{-3} \int_0^\delta \epsilon dz$
500	479	0.0619	25.5	0.66	0.88	1.31
750	886	0.0561	21.0	0.65	0.90	1.34
1000	1403	0.0530	18.8	0.62	0.92	1.30
1300	2122	0.0501	17.9	0.59	0.85	1.24
1600	2978	0.0482	17.2	0.61	0.91	1.21

by replacing the mean value of the three-dimensional velocity fields by the time mean over a whole inertial oscillation. Second, high accuracy is also needed in terms of the statistical convergence of averages, bulk measures and large-scale structures; this requires a domain size  $L_x > \mathcal{O}(\delta_{95})$ . We use here  $L_x = L_y = 1.08\Lambda$  for cases with  $Re \leq 1000$  and  $L_x = L_y = 0.54\Lambda$  for  $Re \geq 1300$  which corresponds to  $L_x/\delta_{95} \approx 25$  for  $Re_D = 500$  and  $L_x/\delta_{95} \approx 18$  for  $Re_D = 1300$ .

Bulk parameters of the simulations are given in Tab. 2. The surface stress is characterized by  $u_*$  and  $\alpha_*$  in relation to the geostrophic wind vector and discussed in more detail as the drag law below in Sec. 4.1 (we find the expected slight decrease of  $u_*$  and  $\alpha_*$  with increasing  $Re$ ). The boundary-layer height estimated from the 95% stress reduction,  $\delta_{95}$ , is around  $0.6\delta$  to  $0.66\delta$ . Interestingly, the integrated TKE  $\int_0^\delta \epsilon dz$  stays constant when normalized by the friction velocity  $u_*$  while the integrated dissipation  $\int_0^\delta \epsilon dz$  exhibits inviscid scaling when normalized by the magnitude  $G$  of the geostrophic wind. (TKE and dissipation normalized as  $fG^{-3} \int \epsilon dz$  and  $u_*^{-3} \int \epsilon dz$ , exhibit substantial dependence on  $Re$  for the variation of  $u_*$ .) This indicates that the bulk dissipation is governed by the forcing  $G$ -irrespective of  $Re$ . Changes in  $Re$ , however, affect the level and organization of turbulence, and the parameter representing this dependency is the friction velocity  $u_*$  which describes the turbulence production processes in the surface layer, in particular in the buffer layer.

Velocity profiles in inner and outer units (Fig. 1a,b) are in accordance with previous work (Coleman et al., 1992; Spalart et al., 2008; Spalart et al., 2009; Ansorge and Mellado, 2014; Ansorge, 2019): The profiles of the shear-aligned streamwise velocity component are well-collapsed for  $Re_D > 500$  below  $z^- \approx 0.15$  (circles in Fig. 1a); the case with  $Re_D = 500$  is only transitionally turbulent and there is no distinct inner-outer scale separation. The logarithmic law is appropriate for  $50 < z^+ < 0.15Re_\tau$ , where  $z^+ = Re_\tau z^-$ . While the profiles  $U^{\alpha*+}(z^+)$  diverge between different  $Re$  beyond  $z^- = 0.15$ , the corresponding profiles of the velocity deficit  $(U^{\alpha*}(z^-) - G_1^\alpha)/u_*$  agree closely, irrespective of  $Re$ . This illustrates the inner–outer scale-duality in this external flow with inner scaling being appropriate in the inner layer and outer scaling in the outer layer. Also in the outer layer of the flow,  $u_*$  (not the magnitude the geostrophic wind speed  $G$ ) is the governing velocity scale for inviscid, i.e.  $Re$ -independent, normalization.

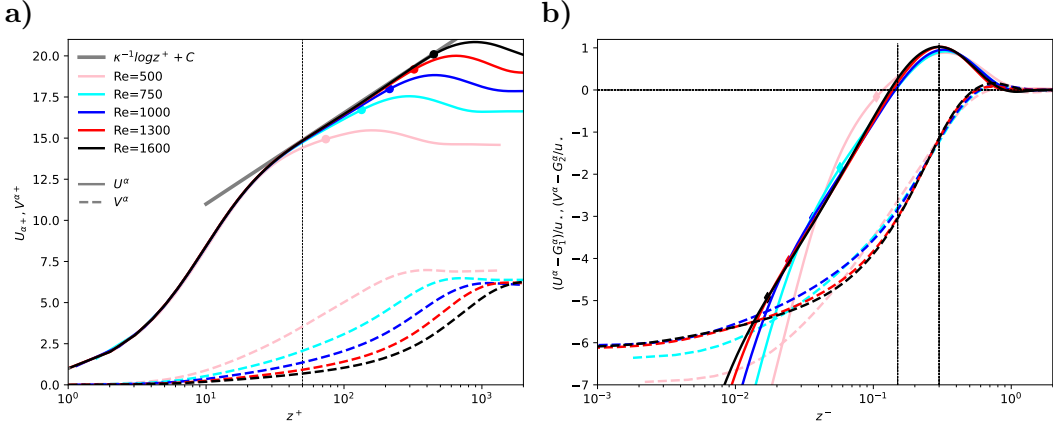


FIGURE 1. a) Shear-aligned velocity profiles in inner units; b) Shear-aligned velocity deficit in outer units; circles mark the height  $z^- = 0.15$ ; dashed line gives the best logarithmic fit to the data.

No collapse in inner units is found for the profiles of spanwise velocity  $V^{\alpha*+}(z^+)$ ; When normalized in outer units, the deficit profiles of spanwise velocity  $(V^{\alpha*}(z^-) - G_2^{\alpha})/u_{\star}$  agree well beyond  $z^- \approx 0.3$ . This is a much higher level in comparison with the streamwise component that collapses also within the overlap layer, i.e. much closer to the surface (circles in Fig. 1b). The value of  $V^{\alpha*+}(z^-) - G_2^{\alpha}$  is sensitive to the wind veering for  $z \rightarrow 0$  as—for use of the shear-aligned component—it has to approach the value  $-G_2^{\alpha} = |G| \sin \alpha \neq 0$  in view of the no-slip boundary condition. While low-Re effects appear to be present for  $\mathcal{O}(\text{Re}) < 10^3$ , the spanwise component converges to an Re-independent limit within the range of scale separation considered here, i.e.

$$(5) \quad G_2^{\alpha}/u_{\star} = Z_{\star} \sin \alpha \rightarrow \text{const. for } \text{Re} \rightarrow \infty,$$

which has indeed already been found by Spalart, 1989, who estimate the constant from an integral relation.

The viscous stress

$$(6a) \quad S_{\text{visc}} = \nu \sqrt{\left( \frac{\partial U}{\partial z} \right)^2 + \left( \frac{\partial V}{\partial z} \right)^2}$$

exhibits universal scaling when considered as  $S_{\text{visc}}^+(z^+)$  (Fig. 2c); this normalization is also appropriate in the outer layer where the viscous stress is, however, small. Small deviations from the universal profile are observed for the smallest Reynolds number  $\text{Re} = 500$ ; we attribute these to low-Re effects in the only transitionally turbulent flow ( $\text{Re}_{\tau} = 479$ ). In contrast to the viscous stress, the total stress follows outer normalization, i.e.  $S^+(z^-)$  is universal; a discrepancy in the inner layer does not occur as the total stress is approximately constant in the viscous and buffer layer, and a rescaling of the height would have no effect there; above, outer scaling is appropriate for the well-established dynamics in the overlap region of inner and outer layer. This, however, implies a mixed scaling for the turbulent stress,

$$(6b) \quad S_{\text{turb}} = \sqrt{\bar{u}w^2 + \bar{v}w^2}.$$

Indeed,  $S_{\text{turb}}$  only follows inner normalization below  $z^+ \lesssim 20$  (where the turbulent contribution is negligible). In the outer layer, where  $S_{\text{visc}} \rightarrow 0$ ,  $S_{\text{turb}}^+$  follows outer

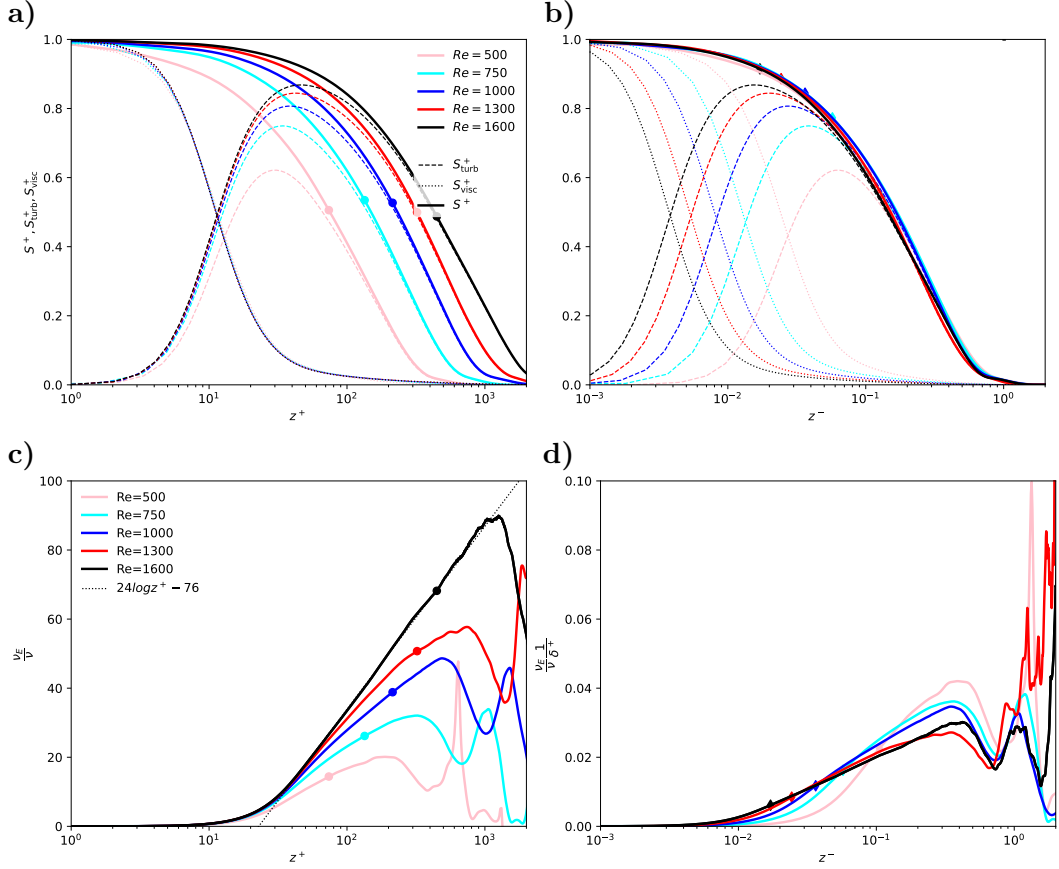


FIGURE 2. **a-b)** Profiles of the turbulent stress  $S_{\text{turb}}^+$  (solid), the viscous stress  $S_{\text{visc}}^+$  (dotted), and the total stress,  $S^+ = S_{\text{visc}}^+ + S_{\text{turb}}^+$  (dashed) as a function of inner height (**a**) and outer height (**b**). **c-d)** Normalized eddy viscosity  $\nu_E$  (solid) plotted versus inner (**c**) and outer height (**d**). Different colors are for different Reynolds numbers (cf. Tab. 1). Circles in (**a**) and (**b**) denote the height  $z^- = 0.15$ , diamonds in (**c**) and (**d**) are for  $z^+ = 50$  as in Fig. 1.

normalization for  $z^- \gtrsim 0.15$ —with increasing accuracy for larger  $\text{Re}$  and larger distance from the surface. In the overlap region, i.e. for  $z^+ > 20$  and  $z^- < 0.15$ , the mixed scaling for the turbulent stress can be expressed as

$$(6c) \quad S_{\text{turb}}^+(z^+, \text{Re}_\tau) = S^+(z^-) - S_{\text{visc}}^+(z^+),$$

where  $z^- = z^+/\text{Re}_\tau$ .

The Eddy viscosity plays a crucial part when modelling profiles and the vertical transport in turbulent flow. In analogy to the Fick-law for molecular diffusion, the eddy diffusivity is the effective diffusivity that yields the turbulent transport  $S_{\text{turb}}$  based on the strain rate. For the symmetries in the flow (horizontal homogeneity, and  $W = 0$ ), it is

$$(7a) \quad \nu_E = \frac{S_{\text{turb}}}{\sqrt{\left(\frac{\partial U}{\partial z}\right)^2 + \left(\frac{\partial V}{\partial z}\right)^2}} = \nu \frac{S_{\text{turb}}}{S_{\text{visc}}}.$$

The inner normalization of  $\nu_E$  is obtained when dividing by the molecular viscosity:

$$(7b) \quad \nu_E^+ = \nu_E/\nu = S_{\text{turb}}/S_{\text{visc}}.$$

Under this normalization, the profiles of eddy viscosity collapse below  $z^+ \approx 20$  with a tendency towards better collapse at higher  $z^+$  (up to  $z^+ \approx 50$  for  $\text{Re} = 1600$ ; Fig. 2b). In the outer layer, the eddy viscosity is characterized by a distinct minimum at  $z^- \approx 0.6 - 0.8$ , and we find that the following mixed normalization of  $\nu_E$  by the geostrophic wind and friction velocity collapses the value of  $\nu_E$  at this minimum (cf. Fig. 2d):

$$(7c) \quad \nu_E^- = \nu_E^+ \frac{1}{\delta^+} = \nu_E \frac{1}{\nu} \frac{\nu}{u_* \delta} = \nu_E \frac{f}{u_*^2}.$$

Substantial variation of the profiles is, however observed below and above this minimum for different  $\text{Re}$  which illustrates that this normalization is probably not generally appropriate across the outer layer.

The organization of the flow is depicted in terms of the turbulence kinetic energy in Fig. 3. In vicinity of the wall, at  $y^+ \approx 10$ , (Fig. 3a), elongated streaks aligned with the surface shear stress dominate. Moving away from the wall, to  $y^+ \approx 150$  (well within the logarithmic region), the structures are larger and more isotropic, but they are still largely aligned with the surface shear stress. In the upper part of the outer layer, around  $y^+ \approx 1000$ , no clear signature of the surface veering direction is found, and intense TKE structures (bright yellow) are organized on a large spatial scale with with weaker eddies (greenish structures) and quiescent regions in between.

#### 4. A UNIVERSAL VELOCITY PROFILE FOR THE TURBULENT EKMAN LAYER

We now turn to the formulation of a general velocity profile that is fully determined by the only parameter of the idealized problem, namely a Reynolds number representing the scale separation or geometric size of the problem. This precludes a drag law wherewith we begin this section (4.1). Based on the scaling arguments put forward in Sec. 3, we then develop a formulation of the wind vector in the Ekman layer (Sec 4.2) and separately for the streamwise (Sec. 4.3) and spanwise (Sec. 4.4) components in the overlap and inner regions.

**4.1. Drag-Law.** A drag-law for Ekman flow determines—as a function of Reynolds number alone—the surface drag. This can be formulated in terms of the modulus of the surface friction normalized by the geostrophic wind forcing,  $u_*$  (Eq. (1b)) and, the direction of surface shear stress,  $\alpha_*$  (Eq. (1c)), also termed wind veering. A non-zero veering of the wind is a rather special case in comparison with most turbulent flows considered in an engineering context, and it confronts us with a situation where the most appropriate coordinate system for analysis (namely that aligned with the surface shear stress) is a priori unknown. We compare our DNS data against a semi-empirical drag-law based on integral consideration Spalart, 1989 and find, as demonstrated in previous work Ansorge and Mellado, 2014, excellent agreement in the range  $400 < \text{Re} < 1600$ , representing a factor of 16 in variation of viscosity.

We also find that the solution of the transient equation involved in estimation of  $u_*$  for a given Reynolds number  $\text{Re}_D$  is approximated reasonably by the formulation

$$(8) \quad u_* = 4 \log(\text{Re}_D) - 8$$

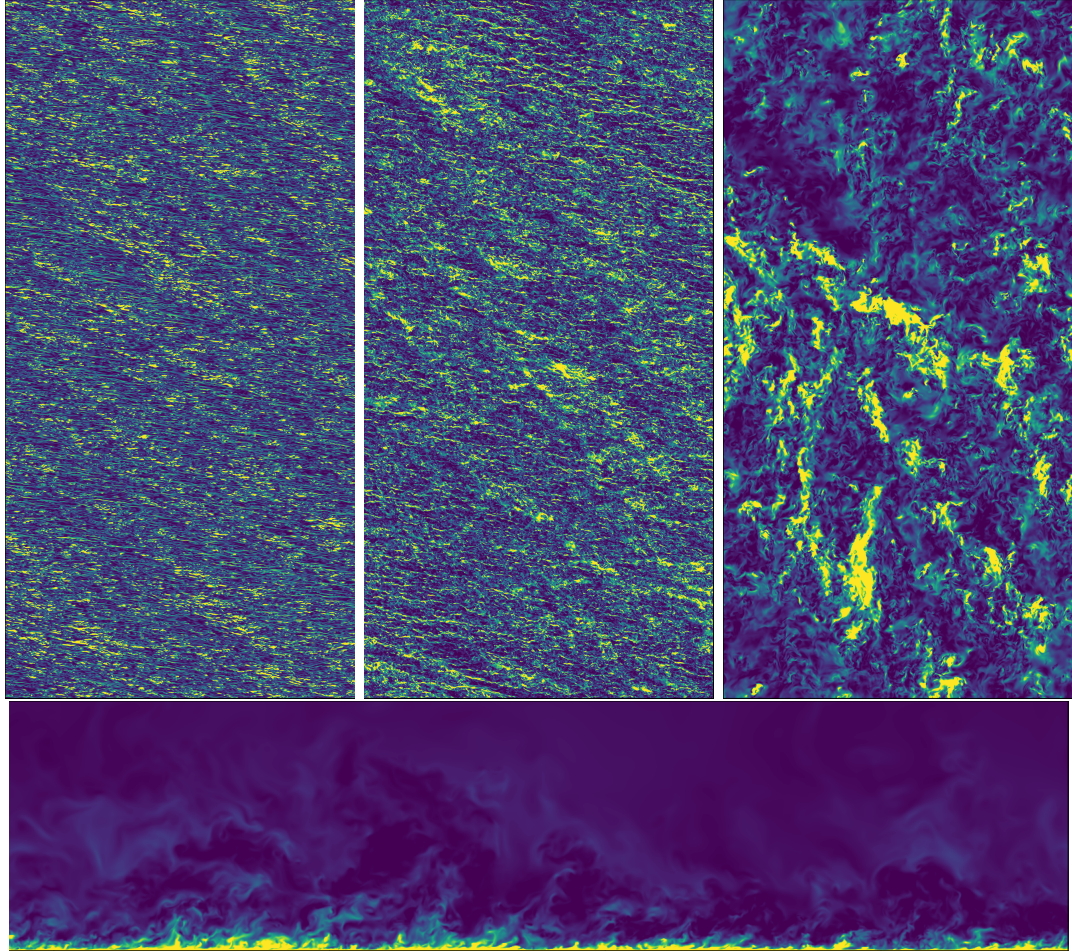


FIGURE 3. horizontal slices of turbulence kinetic energy in the Buffer layer ( $i=10$ ), logarithmic Layer ( $i=100$ ), and outer layer ( $i=400$ ); coloring between percentiles 4 and 96 of the respective image. Lower panel:streamwise–vertical intersect through the domain

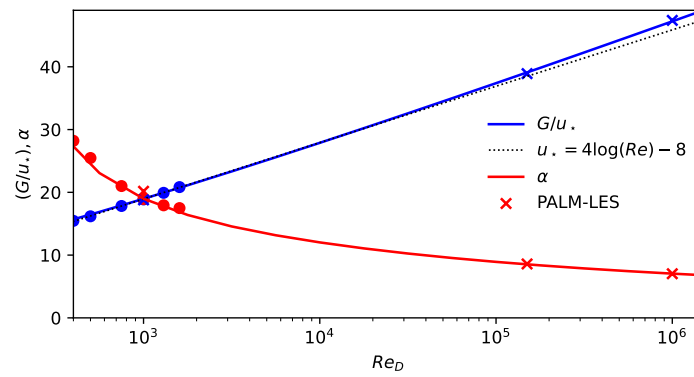


FIGURE 4. Variation of geostrophic drag,  $Z_*$ , and surface veering,  $\alpha_*$ , with Reynolds number according to the theory by Spalart et al. (1989) and as estimated from DNS data

which quantifies the ‘weak’ dependence of  $u_*$  on the Reynolds number as an approximately logarithmic one, at least for problems with a scale separation on the order that is relevant to geophysical problems ( $Re_D < 10^8$ ).

**4.2. Profile in the Ekman layer.** Formulations for the outer layer that take into account the rotation (and thus deviation from the channel-flow analogy) need to be matched to the framework of surface similarity. A smooth transition from the inner layer to the Ekman layer, where the wind is characterized by a turning of its mean direction, is not easily achieved. Optis et al., 2014, for instance, define an “effective geostrophic wind vector that has the same magnitude of the observed surface geostrophic wind and is rotated by the angle  $\alpha$  [their nomenclature]” to overcome the unsteady transition when approaching the Ekman layer from below. Such rotation of the wind vector is *a posteriori* justified by the observational data that the model outcomes are compared to. This need for a connection of the two reference frames is a manifestation of a mismatch in the theoretical treatment of the inner and outer layer in this rotating flow configuration.

The text-book solution for Ekman flow makes use of the physical boundary conditions (BCs) for the atmospheric boundary layer (no-slip at the bottom and geostrophic wind in the free atmosphere) and a constant eddy viscosity. Specifying the boundary conditions at top and bottom eliminates one mode of the analytical solution, and it determines the magnitude of the spiral. In doing so, one has to assume that the solution is appropriate across the entire ABL, which is not the case: The dynamics put forth by Ekman in 1905 are not appropriate in the surface layer of the ABL; better approximations exist for the logarithmic, buffer, and viscous sublayers. In view of this situation, we use an adapted Ekman spiral that does not enforce the boundary conditions at the surface but at a different height. This is achieved by considering the Ekman spiral only in the Ekman layer, thus giving way for the well-established logarithmic and viscous-layer profiles in the lower surface layer. Based on the derivation in App. A, this profile is given by

$$(9a) \quad \frac{1}{G} \begin{pmatrix} U_{ek} \\ V_{ek} \end{pmatrix} = \begin{pmatrix} 1 \\ 0 \end{pmatrix} + e^{-z_{ek}} \left[ a_{ek} \begin{pmatrix} -\cos z_{ek} \\ \sin z_{ek} \end{pmatrix} + b_{ek} \begin{pmatrix} \sin z_{ek} \\ \cos z_{ek} \end{pmatrix} \right]$$

$$(9b) \quad z_{ek} = \delta_{ek}(y^- - s_{ek}).$$

The right-hand-side consists of two modes with magnitude  $a_{ek}$  and  $b_{ek}$  shifted by  $\pi/2$  with respect to each other. In the classic case, the second mode governed by  $b_{ek}$  is incompatible with the surface boundary condition. While this is not the case here for the general form of the profile, we phase shifts can also be captured by the parameter  $s_{ek}$ , and we stick with to a single-modal approach, i.e., we let  $b_{ek} = 0$ .

This single-modal solution is characterized by three parameters, (i) an Ekman-layer depth scale  $\delta_{ek}$ , (ii) the magnitude parameter of the spiral  $a_{ek}$ , and (iii) a zero-crossing point for the velocity  $s_{ek}$ . The effects of varying these parameters are illustrated in Fig. 5 where the classic Ekman solution is recovered by setting  $a_{ek} = 1$ ,  $s_{ek} = 0$  and  $\delta_{ek} = \sqrt{2\nu/f}$ . These parameters are *a priori* unknown as they need to conform to the turbulent state of the boundary layer; we use our DNS data to arrive at best estimates for them.

**The Ekman-layer depth scale**  $\delta_{ek}$  is fundamentally defined by the eddy viscosity. However, we have seen in Section 3 that a characteristic value for the eddy diffusivity is not easily obtained for its strong dependence on the Reynolds number

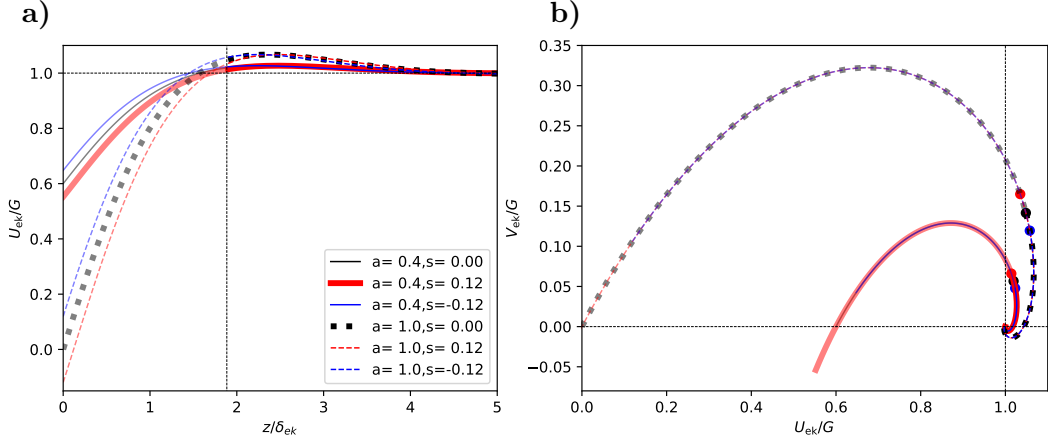


FIGURE 5. **a)** Generalized Ekman-profile of the geostrophic-aligned component  $U_{ek}$ . **b)** Hodograph for the geostrophic-aligned and pressure-gradient aligned components  $U_{ek}$  and  $V_{ek}$ . Thick, black dashed line shows the classic solution. The height corresponding to  $z^- = 0.30$  is marked by the dashed line in panel (a) and by filled circles in panel (b). The hodograph and profiles above this reference height are shown as solid lines, below as opaque line.

and distance from the surface. We therefore resort to the physical manifestation of the eddy diffusivity in an Ekman layer, and use the boundary layer depth  $\delta_{ek} = 0.66\delta \times 2\pi$ . For the relation  $\delta_{ek} = \sqrt{2\nu_{ek}/f}$ , this yields  $\nu_{ek} \propto u_*^2/f$  in accordance with the observations in Sec. 3 (Eq. 7c).

**The magnitude parameter of the Ekman spiral**,  $a_{ek}$ , defines the super-geostrophic maximum of the wind profile aloft the logarithmic layer. Our simulations suggest this maximum of the velocity deficit remains constant when normalized by  $u_*$  as shown in Fig. 6. The numerical value of  $a_{ek}$  is estimated from visual comparison, and we find  $a_{ek} = 8.4u_*$ ; while this appears rather large, it is pre-multiplied by  $e^{-z_{ek}}$  which has already decreased to  $\mathcal{O}(0.1)$  at the height of this maximum. This choice ascertains that the velocity deficits  $U/u_* - Z_*$  and  $V/u_* - Z_*$  do not depend on the velocity scale  $u_*$ , but only on  $G$  as

$$(10) \quad U_{ek}/u_* - Z_* \propto a_{ek}Z_* = 8.4G.$$

Thus, the reduction of the area under the Ekman hodograph is directly linked to the variation in the friction velocity, which quantifies the well-known qualitative observation that a more turbulent boundary layer leads to a flatter hodograph in Ekman flow.

**The offset parameter**  $s_{ek}$  defines the zero-crossing height of the profile (in contrast to  $\delta_{ek}$ , which determines the thickness across which the wind veering takes place). Physically, this offset can be understood as the height at which the surface was located assuming a perfect Ekman flow down to the surface. As this is not the case, and gradients are steeper in the highly turbulent boundary layer flow encountered when approaching the surface, the offset is smaller than zero (the fully turbulent boundary layer is actually thinner than an Ekman layer would be). From our DNS data, we estimate  $s_{ek} = -0.12$ .

In summary, the outer layer of Ekman flow is characterized by a turning of the wind velocity and the super-geostrophic maximum that is sustained by momentum convergence at the inflection point of the velocity profile. The super-geostrophic

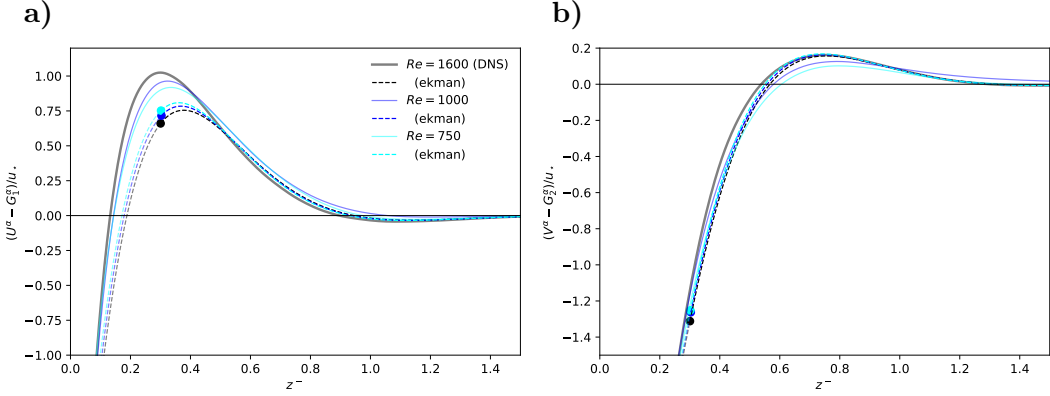


FIGURE 6. Shear-aligned velocity deficit for the wall-streamwise (panel (a)) and wall-spanwise (panel (b)) components of the mean velocity  $U^\alpha$  and  $V^\alpha$ . Solid lines show DNS data, dashed lines the Ekman profiles  $U_{\text{ek}}$  and  $V_{\text{ek}}$  as defined in Eq. 9. Region below  $z^- = 0.3$  is shown opaque. Variations in  $U_{\text{ek}}$  and  $V_{\text{ek}}$  are a consequence of the normalization and related to changes in  $u_*$  and  $\alpha_*$  among the different  $Re_D$ .

maximum of streamwise velocity and a secondary minimum aloft the bulk-turbulent part of the boundary layer are well-described by a classic Ekman spiral with adapted boundary conditions and a shift in reference height. Corresponding profiles are shown in comparison with data from three DNS runs in Fig. 6. The idealized profiles capture the secondary minimum and convergence to the geostrophic equilibrium in the non-turbulent flow very well.

**4.3. Streamwise Velocity Component.** For the streamwise velocity profile (that in non-rotating flows due to the geometry is always aligned with the surface shear stress), well-established theories exist for various regimes according to their distance from the wall and the relative role of viscosity, turbulence and interaction with the outer region of the flow with the logarithmic law for the mean velocity as a central anchor point.

In immediate vicinity to the surface, local turbulent mixing cannot occur for the no-slip/no-penetration boundary condition, and the mean velocity is described by a viscous profile of the form

$$(11a) \quad U^{\alpha*+} = z^+$$

where the direction of the velocity points into the exact opposite direction of the wall shear stress  $\tau$ . In absence of roughness elements and for small roughness ( $z_0^+ < 5$ ), this linear regime is known as viscous sub-layer Foken, 2002; Foken et al., 1978. In fact, this law of the wall has no degree of freedom given the drag, i.e. once  $u_*$  and  $\alpha_*$  are defined. However, theoretical foundation is lacking for the exact shape of the velocity profile in the buffer layer; though crucial for turbulence production, it is commonly understood as a transition region between the linear profile at the surface and the logarithmic profile aloft. A pure blending from the linear velocity profile into the logarithmic one is, however, not reasonable as both the linear and logarithmic profile overestimate the velocity in the buffer layer. We therefore introduce a higher-order compensating term into the linear profile before blending it into the logarithmic

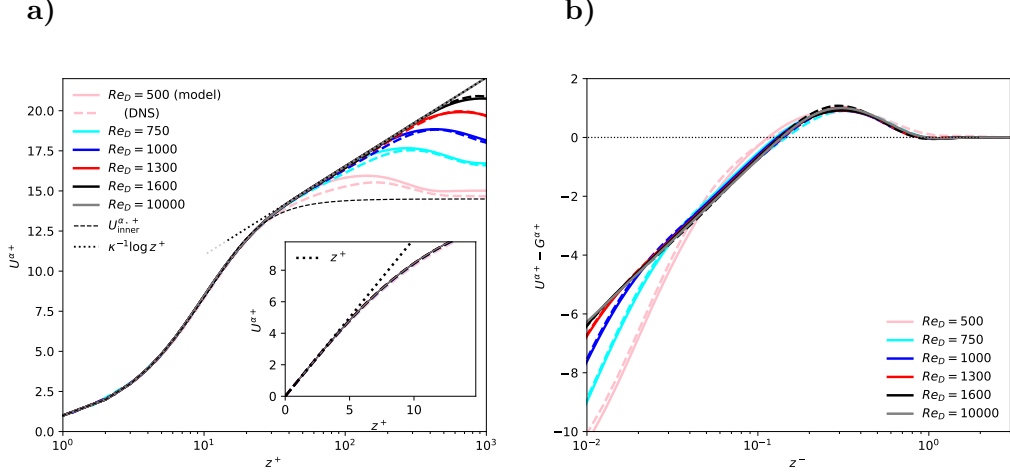


FIGURE 7. Shear-aligned profiles of velocity components  $U^{\alpha*+}$  in inner (left) and outer (right) units.

law:

$$(11b) \quad U_{\text{inner}}^{\alpha*+} = f_{U,\text{visc}}(z^+) = \frac{z^+ + \gamma_4(z^+)^4 + \gamma_6(z^+)^6}{1 + \gamma_6/u_{\text{ref}}(z^+)^6},$$

where the fourth- and sixth-order terms in the nominator are designed to fit the profile below  $y^+ \approx 10$  and the sixth-order correction in the denominator limits the growth of  $u_{\text{inner}}$  for large  $y^+$ . These correction terms are small for  $z^+ < 5$  where the linear law of the wall (shown in the inset in Fig. 7) yields an excellent fit of the data; we use here

$$\gamma_4 = -3.825 \times 10^{-4}; \quad \gamma_6 = 6.320 \times 10^{-6}; \quad u_{\text{ref}} = 1.278 \times 10^1.$$

In the logarithmic region, we use the profile

$$(11c) \quad U_{\log}^{\alpha*+} = \frac{1}{\kappa} \log y^+ + C$$

with the von-Kármán constant  $\kappa = 0.416$  and the boundary condition  $C = 5.4605$ .

**4.4. Spanwise velocity component.** The background rotation and associated veering of the surface wind implies a non-zero profile for the span-wise velocity which challenges the conventional assumptions related to the channel-flow analogy: While the analogy with channel flow in vicinity of the wall implies that the streamwise component be zero or at least small, the veering requires a value of  $V_{top} = U_G \sin \alpha_*$  in the free stream (and thus also at the top of the boundary layer if we assume that any substantial velocity gradient is confined to the turbulent part of the flow). This continuous rotation of the wind vector is conveniently visualized by velocity hodographs aligned with the outer, geostrophic flow (cf. Fig. 5b) and normalized by the geostrophic wind. The geometry of the flow and its drag imply the following for any hodograph: (i) the boundary conditions at the surface, (ii) the boundary condition at the top, and (iii) the inclination of the hodograph at the origin by the

surface veering:

$$(12a) \quad V^{\alpha_*}(z=0) = 0,$$

$$(12b) \quad \lim_{z \rightarrow \infty} V^{\alpha_*} = G \sin \alpha_*$$

$$(12c) \quad \partial_{z+} V^{\alpha_*+}|_{z=0} = 0.$$

Outer scaling of the velocity profile further implies that the velocity deficit of  $(V^{\alpha_*} - G^{\alpha_*})/u_*$  be a universal function of the outer height  $z^-$ . In the outer region of the flow (for  $z^- \mapsto 1$ ),  $f_V(z^-)$ , should govern the spanwise velocity profile, as is supported by our DNS data (Fig.1b); above  $z^- \approx 0.3$ , this profile is very well approximated by the Ekman-turning derived above (Eq. (9); Fig. 6b). While this deficit is a signature of outer rotation, it is inappropriate to extend this general relation to the surface where inner scales matter: On the one hand, the variation of the spanwise velocity deficit across the boundary layer (i.e. between  $0 < z^- < 1$ ) must match the difference implied by the drag law ( $u_*, \alpha_*$ ) and the constant value of  $V^{\alpha_*}$  around  $z^- = 0.3$ . On the other hand,—provided the outer velocity deficit is Re independent—the Re-dependence of  $\alpha_*$  and  $u_*$  implies that this difference cannot be constant as a function of Re

We hence ask, how does the span-wise component scale when the surface is approached? Clearly, the spanwise contribution is small in comparison with the streamwise component throughout much of the layer below  $z^- \approx 0.3$ . However, we cannot assume  $V = 0$  if a smooth matching between the inner and outer layers shall be achieved. In this context, we first realize that the velocity deficit  $(V^{\alpha_*} - G^{\alpha_*})/u_*$  approaches a Re-independent constant around  $C_{V0} = Z_* \sin \alpha - 6.1$  at the surface; deviations from this constant are only found for the lowest Reynolds numbers which is in accordance with the low-Re correrection suggested by Spalart, 1989. This constrains the wind veer, and it quantitatively shows that the decreasing wall friction manifest in an increase of  $Z_*$  exactly compensates the decrease of wind turning measured by  $\sin \alpha_*$ .

If the difference across the boundary layer is constant ( $C_{V0}$ ) vs. Re, the averaged gradient  $\partial_{z+} V^{\alpha_*+}$  of the spanwise velocity component must decrease as  $1/\delta^+$  with increasing  $Re_\tau$ . Hence, it should—at a fixed height—be  $V^{\alpha_*} \propto (\delta^+)^{-1}$ . A profile that agrees with the constraints of the profile at the surface and exploits the dependence of  $V^{\alpha_*}$  on  $\delta^+$  is

$$(13) \quad V^{\alpha_*} \frac{\delta^+}{G} = f_{V,\text{visc}}(z^+) = v_{\text{ref}} (\omega_v z^+ - 1 + \exp[-\omega_v z^+]),$$

where  $v_{\text{ref}}$  controls the magnitude of the profile and  $\omega_v$  sets the height at which the profile transitions into an approximately linear one. We find excellent agreement with the DNS data for  $500 \leq Re_D \leq 1600$  below  $z^+ \approx 15$  with

$$v_{\text{ref}} = 18.85; \quad \omega_v = 0.2353$$

(cf. Fig. 8b).

For the adjacent surface layer, we find a log-like transition from the quasi-linear profile inner profile around  $z^+ = 10$  to a linear profile with increasing Re (Fig. 8b). We model this transition by

$$(14) \quad f_{V,\log}(z^+) = \frac{V_{\log}(z^+)}{G} \delta^+ = a_{\log} + b_{\log} \log z^+ + c_{\log} z^+.$$

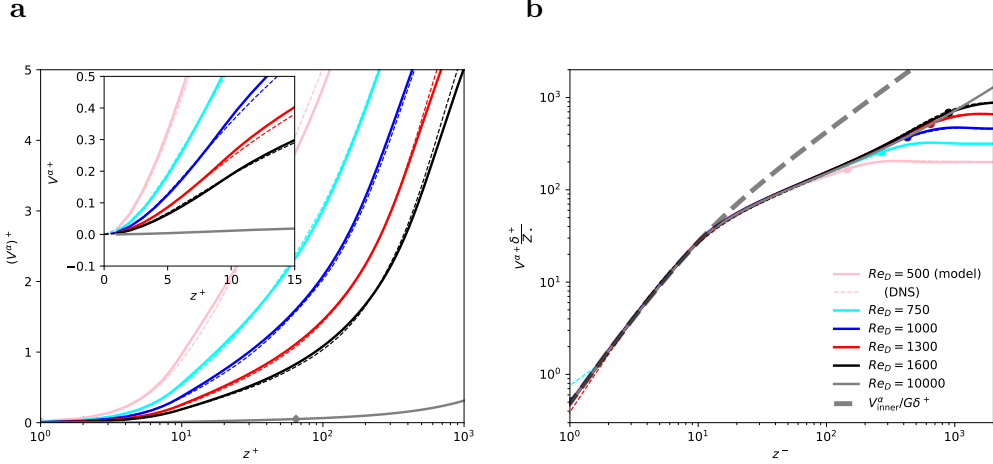


FIGURE 8. Profiles of shear-aligned span-wise velocity  $(W^\alpha)^+$  versus inner height. Dashed lines show DNS data, thick, opaque lines are from the semi-empirical theory developed above. Left panel show standard inner normalization. Right panel shows the inviscid normalization yielding a universal profile for the spanwise component of velocity in the inner layer.

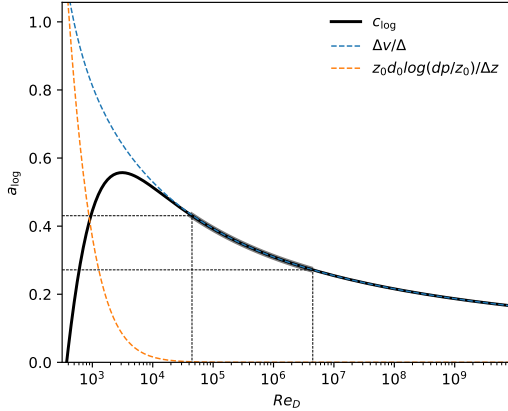


FIGURE 9.  $c_{\log}$ .

This surface-layer profile matches the inner (viscous) scaling in vicinity of the surface to the outer (Ekman) scaling above  $z^- = 0.3$  when constrained by the viscous profile at the bottom and the Ekman profile at the top:

$$(15) \quad f_{V,\log}(z^+ = 10) = \quad f_{V,\text{visc}}(z^+ = 10) =: \quad v_{10} \simeq 27.3$$

$$(16) \quad \frac{\partial}{\partial z^+} [f_{V,\log}]_{z^+ = 10} = \quad \frac{\partial}{\partial z^+} [F_{V,\text{visc}}]_{z^+ = 10} =: \quad d_{10} \simeq 4.01$$

$$(17) \quad f_{V,\log}(z^+ = 0.3\delta^+) = \quad V_{\text{ek}}^{\alpha*}(z^- = 0.3)\delta^+ =: \quad v_{03}$$

where  $v_{03}$  is determined by  $V_{\text{ek}}(0.3)$  and  $U_{\text{ek}}(0.3)$  and depends on  $\text{Re}$ . While the  $\text{Re}$ -dependency of  $a_{\log}$ ,  $b_{\log}$ ,  $c_{\log}$  is small, it shows up in Fig. 1 where the normalized profiles of spanwise velocity become more convex with increasing  $\text{Re}$ . We can now quantify this effect by means of the change of  $c_{\log}$  versus  $\text{Re}$  which is shown in Fig. 9 (cf. Appendix B;  $a_{\log}$  and  $b_{\log}$  are then determined by the universal values of  $v_{10}$  and  $d_{10}$ ).

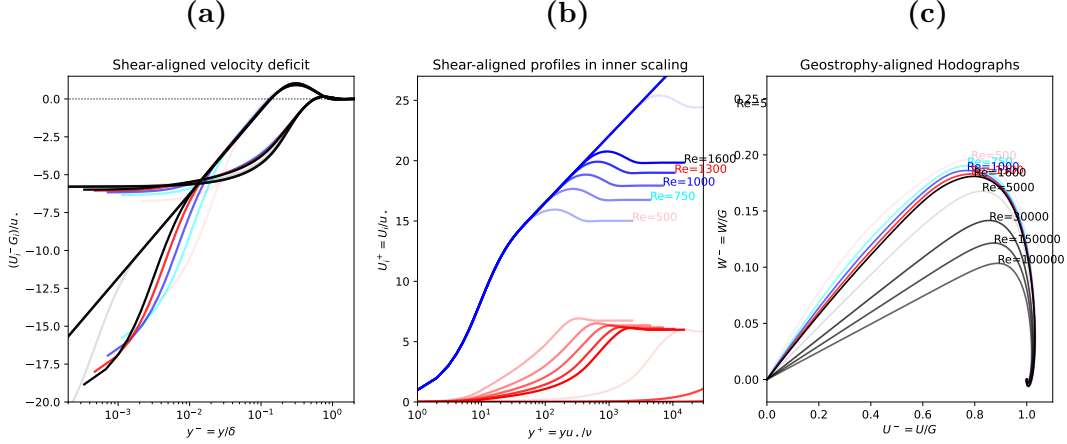


FIGURE 10. (a) Velocity deficit, (b) velocity profile in shear-aligned hodographs and (c) hodograph in geostrophy-aligned coordinates. Thick, solid lines show theory, dashed lines data from DNS.

**4.4.1. Discussion.** Eq. (13) establishes a universal mixed scaling for the spanwise velocity in the viscous layer: While it requires the vertical coordinate to be expressed in inner units, the velocity itself is normalized by the geostrophic wind, and becomes inversely proportional to the friction Reynolds number  $\text{Re}_\tau = \delta^+$  when considered at a fixed height. In vicinity of the surface, such mixed scaling has already been identified for higher-order statistics in convective flows (Mellado et al., 2016; Li et al., 2018), where large scales leave their signatures in vicinity of the surface. It is important to note here that, while  $V$  is a first-order statistic from a statistical perspective, the spanwise velocity is a higher-order correction term from the perspective of similarity theory and from the viewpoint of the channel-flow analogy that is routinely employed in the surface layer. Further, this is consistent with the scaling for the velocity hodograph found in Eq. (10) where the friction velocity also drops out.

In the surface layer, there is not only a mixed scaling—as we had already identified in the viscous layer—but we cannot find a universal function onto which the profiles of spanwise velocity collapse. This additional degree of freedom reflects the inner–outer matching problem for the spanwise velocity, and rather than giving a universal profile for this region, as is usually done, we resort here to a parametric description of the problem, namely in terms of the function  $f_{V,\log}$  determined by the parameters  $a_{\log}$ ,  $b_{\log}$ ,  $c_{\log}$  which can be estimated based on the above scaling considerations for any Reynolds number. We note that, once the parameter  $a_{\log}$  is known, the parameters  $b_{\log}$  and  $c_{\log}$  can be estimated solely based on  $f_{V,\text{visc}}$ , i.e. using the value  $v_{10}$  and  $d_{10}$  found for the viscous region of the flow. For the range of Reynolds number relevant to geophysical problems ( $10^4 \lesssim \text{Re}_D \lesssim 10^6$ ), the variation of  $c_{\log}$  is, however, rather small.

## 5. COMPARISON WITH OTHER THEORIES

**Compare** to Emeis (2002) and Gryning (2007); highlight explicit knowledge on veering-profile → directional sheer;

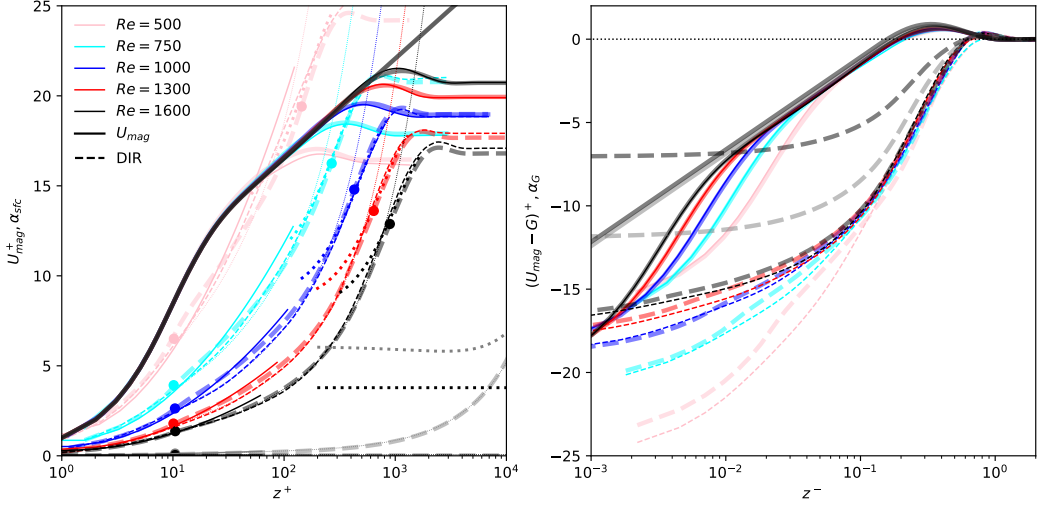


FIGURE 11. Total velocity and veering (in degrees) vs inner and outer height.  
Dashed lines show DNS data, thick lines are from semi-empirical theory.

Implications for **K-theory** (we now can consider that shear and stress are not necessarily perfectly aligned). → can we do something to infer a K-profile from these theoretical considerations?

## 6. CONCLUSIONS

Applications:

- reference-shear for neutral profile approaches(systematic!) → wind engineering!
- initial condition for LES/DNS to eliminate/minimize inertial oscillation in Benchmark simulations
- 

## APPENDIX A. LAMINAR EKMAN SOLUTION WITH CONSIDERATION OF INNER LAYER

$$(13a) \quad \begin{pmatrix} \partial_t U \\ \partial_t W \end{pmatrix} = \begin{pmatrix} fW & + \nu \partial_z^2 U \\ -f(U - G) & + \nu \partial_z^2 W \end{pmatrix}$$

$$(13b) \quad \Rightarrow \partial_t(U + iW) = f(W - i(U - G)) + \nu \partial_z^2(U + iW)$$

In stationary conditions, this system is solved by

$$(13c) \quad \hat{u}(z) = U_\infty + e^{-\gamma z} [A \cos \gamma z + B \sin \gamma z]$$

$$(13d) \quad \hat{w}(z) = W_\infty + e^{-\gamma z} [-A \sin \gamma z + B \cos \gamma z]$$

where the constants  $U_\infty, W_\infty$  set the top boundary condition and  $A$  and  $B$  set the bottom boundary condition. The most common boundary condition for a surface Ekman layer is  $A = U_\infty = G$ ,  $B = 0$ , and  $W_\infty = 0$ . The lower boundary condition, however, neglects the existence of the surface layer, and it appears reasonable to define  $A = cG$  where  $c < 1$  is a constant that incorporates the increased shear in

the surface layer. Given a 'matching height'  $z_{\text{match}}$  and normalized matching height  $\xi = \gamma z_{\text{match}}$  in the upper part of the inner layer, we can match the Ekman profile to the inner layer by letting

$$(14) \quad \begin{aligned} u(z_{\text{match}}) &\equiv u_{\text{match}} = U_{\infty} + e^{-\xi} [A \cos \xi + B \sin \xi] \\ w(z_{\text{match}}) &\equiv w_{\text{match}} = W_{\infty} + e^{-\xi} [-A \sin \xi + B \cos \xi] \end{aligned}$$

$$(15) \quad \Rightarrow \begin{pmatrix} u_{\text{match}} - U_{\infty} \\ w_{\text{match}} - W_{\infty} \end{pmatrix} = e^{-\xi} \begin{pmatrix} A \\ B \end{pmatrix} \begin{pmatrix} \cos \xi & +\sin \xi \\ -\sin \xi & +\cos \xi \end{pmatrix}$$

(16)

Matching the profile at  $\xi = 0$ , one obtains  $A = \Delta u_{\text{match}}$  and  $B = -\Delta w_{\text{match}}$ ; and when the direction  $Ox$  is aligned with the geostrophic wind, we obtain the textbook-case  $A = |\mathbf{G}|$  and  $B = 0$ .

Otherwise, choosing  $B \neq 0$  allows to introduce a phase shift of the Ekman rotation with respect to the decay of the wind spiral. As, however, in our context, the thickness and position of the spiral can already be controlled by the eddy viscosity and an offset in  $\zeta$ , here we let  $B = 0$ .

## APPENDIX B. MATCHING THE SPANWISE VELOCITY PROFILES IN THE INNER LAYER

The spanwise profile in vicinity of the surface is given by  $V/G = f_{V,\text{visc}} \delta^+$  with

$$(17a) \quad f_{V,\text{visc}} = v_{\text{ref}} (\omega_v z^+ - 1 + e^{-\omega_v z^+})$$

$$(17b) \quad f_{V,\log} = a_{\log} + b_{\log} \log z^+ + c_{\log} z^+$$

Matching the profiles and gradient  $z_0 = 10^+$  and the value at  $z_1 = 0.3^+$  yields

$$(18a) \quad v_{\text{ref}} (\omega_v z_0 + e^{-\omega_v z_0}) = v_0 = a_{\log} + b_{\log} \log z_0 + c_{\log} z_0$$

$$(18b) \quad v_1 = a_{\log} + b_{\log} \log z_1 + c_{\log} z_1$$

$$(18c) \quad v_{\text{ref}} \omega_z (1 - e^{-\omega_z z_0}) = d_0 = \frac{b_{\log}}{z_{10}} + c_{\log}$$

The gradient condition implies  $b_{\log} = (d_0 - c_{\log}) z_0$ , and yields

$$(19a) \quad v_0 - z_0 d_0 \log z_0 = a_{\log} + c_{\log} (z_0 - z_0 \log z_0)$$

$$(19b) \quad v_1 - z_0 d_0 \log z_1 = a_{\log} + c_{\log} (z_1 - z_0 \log z_0)$$

$$(19c) \quad \Rightarrow c_{\log} = \frac{\Delta v - z_0 d_0 \log z_1 / z_0}{\Delta z}$$

with  $\Delta z = z_1 - z_0$  and  $\Delta v = v_1 - v_0$ . Then, the coefficient  $a_{\log}$  is estimated as

$$(19d) \quad a_{\log} = v_0 - z_0 d_0 \log z_0 - \frac{\Delta v - z_0 d_0 \log z_1 / z_0}{\Delta z} [z_0 - z_0 \log z_0].$$

We note that  $\log(z_1/z_0)/(z_1 - z_0) \rightarrow 0$  for large  $z_1$ , and as  $z_1 = 0.3\delta^+$ , this implies that the second term in  $c_{\log}$  only plays a role at low and intermediate Re. Then,  $a_{\log}$  can be estimated as

$$(19e) \quad a_{\log} \simeq v_0 - z_0 \left[ d_0 \log z_0 - \frac{\Delta v}{\Delta z} (1 - \log z_0) \right]$$

for large Re.

## REFERENCES

- Ansorge, C. (2019). "Scale Dependence of Atmosphere–Surface Coupling Through Similarity Theory". en. *Boundary-Layer Meteorology* 170.1, pp. 1–27. DOI: 10.1007/s10546-018-0386-y.
- Ansorge, C. and Mellado, J. P. (2014). "Global Intermittency and Collapsing Turbulence in the Stratified Planetary Boundary Layer". en. *Boundary-Layer Meteorology* 153.1, pp. 89–116. DOI: 10.1007/s10546-014-9941-3.
- (2016). "Analyses of external and global intermittency in the logarithmic layer of Ekman flow". en. *Journal of Fluid Mechanics* 805, pp. 611–635. DOI: 10.1017/jfm.2016.534.
- Baars, W. J. and Marusic, I. (2020). "Data-driven decomposition of the streamwise turbulence kinetic energy in boundary layers. Part 2. Integrated energy and". en. *Journal of Fluid Mechanics* 882, A26. DOI: 10.1017/jfm.2019.835.
- Barenblatt, G. I. (1993). "Scaling laws for fully developed turbulent shear flows. Part 1. Basic hypotheses and analysis". en. *Journal of Fluid Mechanics* 248, pp. 513–520. DOI: 10.1017/S0022112093000874.
- Barenblatt, G. I. and Goldenfeld, N. (1995). "Does fully developed turbulence exist? Reynolds number independence versus asymptotic covariance". en. *Physics of Fluids* 7.12, pp. 3078–3082. DOI: 10/bw2sqz.
- Blackadar, A. K. and Tennekes, H. (1968). "Asymptotic Similarity in Neutral Barotropic Planetary Boundary Layers." *Journal of the Atmospheric Sciences* 25, pp. 1015–1020. DOI: 10.1175/1520-0469(1968)025<1015:ASINBP>2.0.CO;2.
- Coleman, G. N., Ferziger, J. H. and Spalart, P. R. (1992). "Direct Simulation of the Stably Stratified Turbulent Ekman Layer". *Journal of Fluid Mechanics* 244, pp. 677–712. DOI: 10.1017/S0022112092003264.
- Dimotakis, P. E. (2005). "TURBULENT MIXING". *Annual Review of Fluid Mechanics* 37.1, pp. 329–356. DOI: 10.1146/annurev.fluid.36.050802.122015.
- Ekman, V. W. (1905). "On the influence of the earth's rotation on ocean currents". *Ark. Mat. Astron. Fys.*, Vol. 2 (1905), pp. 1–53. 2, pp. 1–53.
- Emeis, S. (2018). *Wind Energy Meteorology*. 2nd ed. Atmospheric Physics for Wind Power Generation. Heidelberg: Springer.
- Emeis, S. et al. (2007). "Wind and turbulence in the urban boundary layer analysis from acoustic remote sensing data and fit to analytical relations". en. *Meteorologische Zeitschrift* 16.4, pp. 393–406. DOI: 10.1127/0941-2948/2007/0217.

- Esau, I. (2004). "Simulation of Ekman Boundary Layers by Large Eddy Model with Dynamic Mixed Subfilter Closure". en. *Environmental Fluid Mechanics* 4.3, pp. 273–303. DOI: 10/b8f3kh.
- Etling, D. (2002). *Theoretische Meteorologie*. 2nd. Eine Einführung. Berlin, Heidelberg: Springer-Verlag.
- Foken, T., Kitajgorodskij, S. A. and Kuznecov, O. A. (1978). "On the dynamics of the molecular temperature boundary layer above the sea". en. *Boundary-Layer Meteorology* 15.3, pp. 289–300. DOI: 10.1007/BF02652602.
- Foken, T. (2002). "Some aspects of the viscous sublayer". en. *Meteorologische Zeitschrift* 11.4, pp. 267–272. DOI: 10.1127/0941-2948/2002/0011-0267.
- Gryning, S.-E. et al. (2007). "On the extension of the wind profile over homogeneous terrain beyond the surface boundary layer". en. *Boundary-Layer Meteorology* 124.2, pp. 251–268. DOI: 10.1007/s10546-007-9166-9.
- Högström, U. (1988). "Non-dimensional wind and temperature profiles in the atmospheric surface layer: A re-evaluation". *Boundary-Layer Meteorology* 42, pp. 55–78. DOI: 10.1007/BF00119875.
- (1996). "Review of some basic characteristics of the atmospheric surface layer". *Boundary-Layer Meteorology* 78.3-4, pp. 215–246. DOI: 10.1007/BF00120937.
- Jacobs, A. F. and Van Boxel, J. H. (1988). "Changes of the displacement height and roughness length of maize during a growing season". en. *Agricultural and Forest Meteorology* 42.1, pp. 53–62. DOI: 10.1016/0168-1923(88)90066-4.
- Jiang, Q., Wang, S. and Sullivan, P. (2018). "Large-Eddy Simulation Study of Log Laws in a Neutral Ekman Boundary Layer". en. *Journal of the Atmospheric Sciences* 75.6, pp. 1873–1889. DOI: 10.1175/JAS-D-17-0153.1.
- Kelly, M. and Gryning, S.-E. (2010). "Long-Term Mean Wind Profiles Based on Similarity Theory". en. *Boundary-Layer Meteorology* 136.3, pp. 377–390. DOI: 10.1007/s10546-010-9509-9.
- Kelly, M. and Troen, I. (2016). "Probabilistic stability and ‘tall’ wind profiles: theory and method for use in wind resource assessment". *Wind Energy* 19.2, pp. 227–241. DOI: 10.1002/we.1829.
- Li, Q. et al. (2018). "Implications of Nonlocal Transport and Conditionally Averaged Statistics on Monin–Obukhov Similarity Theory and Townsend’s Attached Eddy Hypothesis". en. *Journal of the Atmospheric Sciences* 75.10, pp. 3403–3431. DOI: 10.1175/JAS-D-17-0301.1.
- Marusic, I. et al. (2013). "On the logarithmic region in wall turbulence". en. *Journal of Fluid Mechanics* 716, R3. DOI: 10.1017/jfm.2012.511.

- Mellado, J. and Ansorge, C. (2012). "Factorization of the Fourier transform of the pressure-Poisson equation using finite differences in colocated grids". en. *ZAMM - Journal of Applied Mathematics and Mechanics / Zeitschrift für Angewandte Mathematik und Mechanik* 92.5, pp. 380–392. DOI: 10.1002/zamm.201100078.
- Mellado, J. P., Heerwaarden, C. C. van and Garcia, J. R. (2016). "Near-Surface Effects of Free Atmosphere Stratification in Free Convection". en. *Boundary-Layer Meteorology* 159.1, pp. 69–95. DOI: 10.1007/s10546-015-0105-x.
- Moin, P. and Mahesh, K. (1998). "Direct numerical simulation: A tool in turbulence research". *Annual Review of Fluid Mechanics* 30, pp. 539–578. DOI: 10.1146/annurev.fluid.30.1.539.
- Monin, A. S. (1970). "The Atmospheric Boundary Layer". *Annual Review of Fluid Mechanics* 2, pp. 225–250. DOI: 10.1146/annurev.fl.02.010170.001301.
- Monin, A. S. and Yaglom, A. M. (1975). *Statistical Fluid Mechanics*. Ed. by J. L. Lumley. Vol. I. Mechanics of Turbulence. Dover Publications, Inc.
- Optis, M., Monahan, A. and Bosveld, F. C. (2014). "Moving Beyond Monin-Obukhov Similarity Theory in Modelling Wind-Speed Profiles in the Lower Atmospheric Boundary Layer under Stable Stratification". *Boundary-Layer Meteorology* 153.3, pp. 497–514. DOI: 10.1007/s10546-014-9953-z.
- Rossby, C.-G. and Montgomery, R. B. (1935). "The layer of frictional influence in wind and ocean currents". *Papers in Physical Oceanography and Meteorology* III.3, pp. 1–101.
- Sakagami, Y., Haas, R. and Passos, J. C. (2020). "Generalized Non-dimensional Wind and Temperature Gradients in the Surface Layer". en. *Boundary-Layer Meteorology* 175.3, pp. 441–451. DOI: 10.1007/s10546-020-00510-3.
- Silva, C. B. da et al. (2014). "Interfacial Layers Between Regions of Different Turbulence Intensity". en. *Annual Review of Fluid Mechanics* 46.1, pp. 567–590. DOI: 10.1146/annurev-fluid-010313-141357.
- Spalart, P. R. (1989). "Theoretical and numerical study of a three-dimensional turbulent boundary layer". en. *Journal of Fluid Mechanics* 205.-1, p. 319. DOI: 10.1017/S0022112089002053.
- Spalart, P. R., Coleman, G. N. and Johnstone, R. (2008). "Direct numerical simulation of the Ekman layer: A step in Reynolds number, and cautious support for a log law with a shifted origin". en. *Physics of Fluids* 20.10, p. 101507. DOI: 10.1063/1.3005858.
- (2009). "Retraction: "Direct numerical simulation of the Ekman layer: A step in Reynolds number, and cautious support for a log law with a shifted origin" [Phys. Fluids 20, 101507 (2008)]". en. *Physics of Fluids* 21.10, p. 109901. DOI: 10.1063/1.3247176.

- Stoll, R. et al. (2020). “Large-Eddy Simulation of the Atmospheric Boundary Layer”. en. *Boundary-Layer Meteorology* 177.2-3, pp. 541–581. DOI: 10/gmbmzw.
- Tennekes, H. (1973). “The Logarithmic Wind Profile.” *Journal of the Atmospheric Sciences* 30, pp. 234–238. DOI: 10.1175/1520-0469(1973)030<0234:TLWP>2.0.CO;2.
- Zikanov, O., Slinn, D. N. and Dhanak, M. R. (2003). “Large-eddy simulations of the wind-induced turbulent Ekman layer”. en. *Journal of Fluid Mechanics* 495, pp. 343–368. DOI: 10/ccbpbw.

## APPENDIX A. OLD STUFF

**[OLD FROM HERE]** Below this region, the gradients in span-wise velocity are rather small and the span-wise velocity monotonically approaches its surface boundary condition  $V(z = 0) = 0$ . While the streamwise velocity follows a universal inner scaling that has acquired its universal,  $Re$ -independent shape for  $Re_D > \mathcal{O}(10^3)$ , the span-wise component that defines how the velocity vector veers when the surface is approached, does not collapse in inner units, and there is, most importantly no sign of convergence even at the highest Reynolds numbers for which simulations were carried out. Even though the simplest assumption  $V = 0$  is reasonable for the lower part of the surface surface layer ( $z^- < 10^{-3}$ ), it does not appropriately capture the profile in the rest of the surface layer:

First,  $V = 0$  implies a discontinuity in the velocity profile at  $z^- = 0.1$ , where the outer scaling found above yields a finite value at geophysical  $Re$ , i.e. there is non-zero veering in the upper part of the surface layer—as is well-known also from field observation. Second, the layer around  $z^- = 0.1$  is crucial to obtain the characteristic and well-established shape of the hodographs as the layer where  $V$  sets in marks the ‘maximum’ of  $V^-$  vs.  $U^-$ .

The scale for the magnitude of the span-wise velocity component is  $u_* \sin \alpha$ . Based on our DNS data, we suggest that the Reynolds number scaling of this velocity-magnitude scale is captured by  $Re_\tau^{-1/2}$  which is indeed known from the generalization of higher-order statistics, such as turbulent fluxes in the inner layer (Marusic et al., 2013) that also follow a mixed scaling in the inner layer. We then parameterize the spanwise velocity at 10 wall units as anchor point in the inner layer:

$$(20a) \quad V_{10} \equiv V(z^+ = 10) = 750 \frac{u_* \sin \alpha}{\sqrt{Re_\tau}}.$$

This leaves us with three fixed points of the velocity profile in the inner layer, namely (i) the boundary condition  $V_0 = 0$ , (ii)  $V_{10}$  at  $z^+ = 10$ , and (iii) the lower end of the logarithmic profile at  $z^- = 0.1$  where the latter two are semi-empirically estimated from DNS data. In absence of well-established scaling considerations for the span-wise velocity, the choice of profile fits joining these three points is indeed arbitrary, but we can resort to the DNS data for an empirical approach and find that a square-root profile fits  $V(z^+)$  in the surface layer. A linear profile for  $V$  is employed in the viscous sub-layer. Based on the physical extent of the viscous sub-layer in Ekman flow around five wall units (Foken, 2002; Ansorge, 2019), we choose  $z^+ = 5$  to transition from one to the other and note that  $V$  is already very small at

this height. The span-wise velocity profile in the surface layer is then estimated as

$$(20b) \quad V(z^+)|_{\text{inner}} = \begin{cases} a_1 z^+ & ; \quad z^+ \leq 5 \\ b_1 + b_2 \sqrt{z^+} & ; \quad 5 < z^+ < Re_\tau/10 \end{cases},$$

with  $b_1$  and  $b_2$  estimated such that

$$(20c) \quad \begin{aligned} V(z^+ = 10)|_{\text{inner}} &= V_{10} \\ V(z^+ = Re_\tau/10)|_{\text{inner}} &= V_{\text{outer}}(0.1) \end{aligned} \Rightarrow \begin{cases} b_2 = \frac{V_{\text{outer}}(0.1) - V_{10}}{\sqrt{Re_\tau/10} - \sqrt{10}} \\ b_1 = V_{10} - \sqrt{10}b_2 \end{cases}$$

We then estimate  $\alpha$  from the matching condition at  $z^+ = 5$ , i.e.

$$(20d) \quad 5a = b_1 + \sqrt{5}b_2 \Rightarrow a = \frac{1}{5} \left[ V_{10} + (\sqrt{5} - \sqrt{10}) \left( \frac{V_{\text{outer}} - V_{10}}{\sqrt{Re_\tau/10} - \sqrt{10}} \right) \right].$$

Matching region. While the profile composed of  $V_{\text{inner}}(z^+ \leq 0.1Re_\tau)$ ,  $V_{\text{outer}}(z^- > 0.1)$  is continuous, it is not smooth at  $z^- = 0.1$ , i.e. at the transition from power-law ( $V \propto \sqrt{z^+}$ ) to logarithmic scaling. To alleviate this issue, we use a second-order polynomial for transition from the inner to the outer layer in the range  $z_{\text{low}} < z < z_{\text{up}}$  such that

$$(20e) \quad V_{\text{trans}}(z^-) = V_{\text{inner}}(z_{\text{low}}^+) + \Delta V (az_{\text{arg}} + b(z_{\text{arg}})^2)$$

with  $\Delta V = V_{\text{outer}}(z_{\text{up}}^-) - V_{\text{inner}}(z_{\text{low}}^+)$  and  $z_{\text{arg}} = (z - z_{\text{low}})/(z_{\text{up}} - z_{\text{low}})$ . It is  $a + b = 1$  for  $V_{\text{trans}}(z_{\text{up}}^-) = V_{\text{outer}}(z_{\text{up}}^-)$ , and we constrain  $a$  by

$$(20f) \quad \frac{\partial V_{\text{trans}}}{\partial z^-} \Big|_{z=z_{\text{low}}} = \frac{\partial V_{\text{inner}}}{\partial z^-} \Big|_{z=z_{\text{low}}},$$

where we find that  $z_{\text{low}}^- = 0.06$  and  $z_{\text{up}}^- = 0.13$  yield satisfactory agreement with DNS data.